Comparative Heliophysics Program
Summer 2016 at NASA Ames Research Center

MULTI-FLUID MODELING OF THE EARTH'S MAGNETOSPHERE

ALEJANDRO ALVAREZ LAGUNA[1,2], NAGI N. MANSOUR[3], ANDREA LANI[2], STEFAAN POEDTS[2]

[1]Centre for mathematical Plasma Astrophysics (CmPA),
KU Leuven
Celestijnenlaan 200B, B-3001 Leuven, Belgium
e-mail: alejandro.alvarez.laguna@vki.ac.be

[2]Aeronautics and Aerospace Department,
von Karman Institute for Fluid Dynamics
Chausse de Waterloo, 72, B-1640 Rhode-St-Gense, Belgium

[3]NASA Ames Research Center
Moffett Field, CA 94035-1000, USA

Key words: Plasma physics; two-fluid; magnetic reconnection; Earth's magnetosphere; linear waves; finite volume

Abstract. We present a computational model for the Earth's magnetosphere that relies on the multi-fluid plasma model. When the multi-fluid equations are coupled to the full Maxwell's equations, the resulting system is able to tackle non-equilibrium effects that are beyond the magnetohydrodynamics (MHD) description. The multi-fluid model allows for studying relevant phenomena in the Earth's magnetosphere such as the presence of heavier ions, high frequency waves, small scale dynamics, non-thermal equilibrium or separation of the species motion. In this article, the derivation of the multi-fluid model from kinetic theory is presented. The propagation of linear waves in the ideal collisionless two-fluid model under solar wind and magnetospheric conditions is studied. The two-fluid model is implemented using a second order finite volume method. The algorithm is benchmarked against three cases: electromagnetic shock-tube problem, a supersonic plasma flow over a cylinder and over a sphere. The magnetic reconnection occurring in the magnetotail is studied standalone using a two-fluid model. Preliminary results of a two-fluid global magnetosperic simulation are presented.

1 INTRODUCTION

The solar wind is a plasma flow mainly composed of protons (H^+) and electrons (e^-). The composition of heavier ions is usually limited to small quantities (<0.1%), while the

presence of He^{++} can vary from 3% to 6% under normal conditions [13]. However, large enhancement of the He^{++} abundance (up to 30%) has been observed, as sporadic events, associated to radio bursts in the corona [5]. The abundance of heavy ions observed in the magnetosphere is caused by outflow of ions able to escape from the ionosphere through the polar cap, the dayside cusp, the auroral oval and the nightside auroral region. The main component of the heavy ions in the magnetosphere is O^+. The abundance of this element in the magnetosphere has been measured during geomagnetic events by the International Sun-Earth Explorer (ISEE) to be between 40% to 80% of the total amount of ions [17].

Due to the large abundance of oxygen in the magnetosphere, it is a major challenge the development of models able to account for its effects in the global dynamics. The heavy ions change the local properties of the plasma as they have larger gyroradius. Furthermore, their presence modifies the Alfvén speed and the plasma pressure [14]. It is still nowadays an open question the way heavy ions can affect the development of the Kelvin-Helmholtz instability at the low latitude flanks or the topology of reconnection in the magnetotail, triggering tearing instabilities.

Most of the global models describing the interaction between the solar wind and the Earth's magnetosphere [24, 29, 12], like the vast majority of the models used in solar physics, are based on the (single fluid) model of magnetohydrodynamics (MHD). Although this model is a very useful tool able to represent large scale dynamics, it cannot tackle some of the phenomena occurring in the magnetosphere. Recent efforts have been oriented to reproduce 2D global magnetospheric simulation using the hybrid-Vlasov model [26]. However, a domain containing a global magnetospheric representation is too large to carry out a 3D kinetic simulation with the current computational resources available. Models including the effect of the heavy ions but neglecting the effect of the electrons can be found in [9, 28].

We propose the multi-fluid model, solving for mass, momentum and energy conservation equations for the dominant species of the magnetospheric plasma. The model will consider separately the dynamics of protons (H^+) and electrons (e^-). This model can be easily extended to include heavy ions, i.e., O^+ and He^+. The electromagnetic field will be tackled with the full Maxwell's equations. This innovative coupling allows for accounting for high frequency waves as well as charge separation, both effects completely neglected by the MHD approach.

The present article is organized as follows: 1) the general multi-fluid model is derived from kinetic theory, taking special attention on the assumptions that result in the ideal collisionless two-fluid model; 2) the ideal collisionless model is presented both in dimensional and dimensionless form; 3) the propagation of linear waves in the two-fluid plasma is studied under the solar wind and magnetospheric conditions; 4) the finite volume numerical model is presented; 5) the results of the ideal collisionless two-fluid model are presented.

2 DERIVATION OF THE MULTI-FLUID MODEL

Due to the disparity of multi-fluid plasma models that can be found in literature, in the present section, we present the derivation of the multi-fluid model used in this paper. The present section is based on the works of Meier and Shumlak [20], Zhdanov [31], Braginskii [6] and Benilov [2]. We will present first the derivation of the general model, including inelastic collisions, i.e., chemical reactions, but the rest of the work will focus on the ideal two-fluid model considering ions and electrons.

2.1 Kinetic equation

The evolution of the distribution function $f_\alpha(\vec{v}, \vec{x}, t)$ of the species α within a plasma is described by the Boltzmann's kinetic equation.

$$\frac{\partial f_\alpha}{\partial t} + \vec{v} \cdot \vec{\nabla} f_\alpha + \frac{\vec{F}_\alpha}{m_\alpha} \cdot \vec{\nabla}_{\vec{v}} f_\alpha = J_\alpha + \Gamma_\alpha \tag{1}$$

The left-hand side of the kinetic equation represents the substantial derivative in time of the distribution function, whereas the right-hand side is the variations in time of the distribution function due to collisions. The external force, when the plasma is under the effect of electromagnetic fields, can be written as $q_\alpha \left(\vec{E} + \vec{v} \times \vec{B}\right)$, where the electric and magnetic field are denoted as $\vec{E}$ and $\vec{B}$, respectively; q_α is the electric charge and m_α the mass of the particles α.

In the present work, the collision integral, J_α, accounts for binary collisions including both elastic and reactive collisions. Therefore, the collision operator is a sum over the species, as follows:

$$J_\alpha = \sum_\beta J_{\alpha\beta}(f_\alpha, f_\beta) \tag{2}$$

where $J_{\alpha\beta}(f_\alpha, f_\beta)$ is the collision operator of the binary collision between the species α and β. The partial collisional operator for elastic collisions, can be retrieved under the "molecular chaos" assumption, e.g., [31],[27], as follows:

$$J_{\alpha\beta}(f_\alpha, f_\beta) = \int\int \left(f'_\alpha f'_\beta - f_\alpha f_\beta\right) \sigma_{\alpha\beta} |\vec{v}_\alpha - \vec{v}_\beta| d\Omega d\vec{v}_\beta \tag{3}$$

where quantities after collisions are denoted with the superscript $'$, $d\Omega$ is the solid angle of the scattering after the collision, and $\sigma_{\alpha\beta}$ is the cross section of the collision. The derivation of Eq. (3) can be found in [31]. The reactive collisions are accounted by the operator Γ_α.

2.2 Balance equations

Local macroscopic variables can be obtained from the distribution function by integrating over the velocity space. We define the following macroscopic values: number density

n_α, mass density ρ_α, mean velocity $\vec{u}_\alpha$ and temperature T_α.

$$n_\alpha = \int f_\alpha d\vec{v}, \qquad \rho_\alpha = m_\alpha n_\alpha = \int m_\alpha f_\alpha d\vec{v}$$
$$n_\alpha \vec{u}_\alpha = \int \vec{v} f_\alpha d\vec{v}, \qquad \frac{3}{2} n_\alpha k T_\alpha = \mathcal{U}_\alpha = \frac{m_\alpha}{2} \int (\vec{v} - \vec{u}_\alpha)^2 f_\alpha d\vec{v}$$

The equations describing the evolution of macroscopic variables can be obtained from the kinetic equation by taking moments, i.e., integrating over the velocities space of the particles. Consider a variable $\psi_\alpha(\vec{v}_\alpha, \vec{x}, t)$, we define the averaging operator $\langle \cdot \rangle$ as:

$$n_\alpha \langle \psi_\alpha \rangle = \int \psi_\alpha f_\alpha d\vec{v} \tag{4}$$

Therefore, multiplying Eq. (1) by the variable ψ_α and integrate over the velocities, we obtain the following transport equation:

$$\frac{\partial n_\alpha \langle \psi_\alpha \rangle}{\partial t} + \vec{\nabla} \cdot (n_\alpha \langle \psi_\alpha \vec{v}_\alpha \rangle) - n_\alpha \left[\langle \frac{\partial \psi_\alpha}{\partial t} \rangle + \langle \vec{v} \cdot \vec{\nabla} \psi_\alpha \rangle + \frac{1}{m_\alpha} \langle \vec{F}_\alpha \cdot \vec{\nabla}_{\vec{v}} \psi_\alpha \rangle \right] = \sum_\beta \int \psi_\alpha J_{\alpha\beta} d\vec{v} + \int \psi_\alpha \Gamma_\alpha d\vec{v} \tag{5}$$

Let the variable ψ_α be the collisional invariants, i.e., $\psi_\alpha^{(1)} = m_\alpha$, $\psi_\alpha^{(2)} = m_\alpha \vec{v}_\alpha$, $\psi_\alpha^{(3)} = m_\alpha v_\alpha^2$. Note that using those variables, the terms, $\langle \frac{\partial \psi_\alpha}{\partial t} \rangle$ and $\langle \vec{v} \cdot \vec{\nabla} \psi_\alpha \rangle$ vanish. Using the previous collisional invariants in Eq. 5, we obtain mass, momentum and total energy balance equations for the species α :

$$\frac{\partial \rho_\alpha}{\partial t} + \vec{\nabla} \cdot (\rho_\alpha \vec{u}_\alpha) = \dot{\rho_\alpha}, \tag{6}$$

$$\frac{\partial \rho_\alpha \vec{u}_\alpha}{\partial t} + \vec{\nabla} \cdot (\rho_\alpha \vec{u}_\alpha \vec{u}_\alpha + p_\alpha \bar{\bar{I}}) = \vec{\nabla} \cdot \bar{\bar{\pi}}_\alpha + \vec{F}_\alpha + \sum_\beta \vec{R}_{\alpha\beta}^{elastic} + \vec{R}_\alpha^{react}, \tag{7}$$

$$\frac{\partial}{\partial t} \left[\mathcal{U}_\alpha + \rho_\alpha \frac{u_\alpha^2}{2} \right] + \vec{\nabla} \cdot \left[\left(\mathcal{U}_\alpha + \rho_\alpha \frac{u_\alpha^2}{2} \right) \vec{u}_\alpha \right] = \vec{\nabla} \cdot (\vec{u}_\alpha \cdot \bar{\bar{\pi}}_\alpha - \vec{q}_\alpha - p_\alpha \vec{u}_\alpha) + \rho_\alpha \vec{F}_\alpha \cdot \vec{u}_\alpha + \sum_{\alpha\beta} \dot{Q}_{\alpha\beta}^{elastic} + \dot{Q}_\alpha^{react}. \tag{8}$$

The transport fluxes are also defined in terms of the distribution function and the peculiar velocity, defined as, $\vec{c}_\alpha = \vec{v}_\alpha - \vec{u}_\alpha$. We recall that the peculiar velocity is measured with respect to the macroscopic velocity of the species α, unlike other models, such as [27, 31], where the peculiar velocities are taken with respect to the heavy particles

mean velocity [27] or the mixture mean velocity [31]. Therefore, we define the following macroscopic transport fluxes:

$$p_\alpha = \frac{1}{3}\int m_\alpha f_\alpha c_\alpha^2 d\vec{v}, \quad \pi_{\alpha_{rs}} = \int m_\alpha f_\alpha c_r c_s d\vec{v}, \quad \vec{q}_\alpha = \frac{1}{2}\int m_\alpha c_\alpha^2 \vec{c}_\alpha f_\alpha d\vec{v}. \tag{9}$$

The relaxation terms due to elastic collisions are defined by means of the distribution function, as follows:

$$\vec{R}_{\alpha\beta}^{elastic} = \int m_\alpha \vec{v}_\alpha J_{\alpha\beta} d\vec{v}, \quad \dot{Q}_{\alpha\beta}^{elastic} = \int m_\alpha v_\alpha^2 J_{\alpha\beta} d\vec{v}. \tag{10}$$

Whereas, the relaxation terms due to reactive collisions are written as:

$$\vec{R}_{\alpha}^{react} = \int m_\alpha \vec{v}_\alpha \Gamma_\alpha d\vec{v}, \quad \dot{Q}_{\alpha}^{react} = \int m_\alpha v_\alpha^2 \Gamma_\alpha d\vec{v}. \tag{11}$$

In the following sections, we will focus on the ideal multi-fluid model. The ideal multi-fluid neglects the transport fluxes, $\pi_{\alpha_{rs}}$ and $\vec{q}_\alpha$, treating the fluids as dissipationless. This simplification is equivalent to consider the distribution functions of the fluids to be Maxwellian, i.e.,

$$f_\alpha^{(0)} = n_\alpha \left(\frac{m_\alpha}{2\pi k T_\alpha}\right)^{3/2} \exp\left[-\frac{m_\alpha(\vec{v}_\alpha - \vec{u}_\alpha)^2}{2kT_\alpha}\right]. \tag{12}$$

This simplification holds as long as the dissipation characteristic time is much larger than the hydrodynamic characteristic time.

However, when the transport equation, i.e., Eq. (5), is integrated considering Mawellian distributions, an average transfer of momentum and energy appears as a consequence of the collisions between the species, i.e., $\vec{R}_\alpha^{react}$ and $\dot{Q}_{\alpha\beta}^{elastic}$. Expressions of the average momentum and energy exchange can be found in [2]. When the two latter terms are neglected, the so-called collisionless ideal multi-fluid model is obtained. This simplification holds as long as the collisional characteristic time between the two species is much larger than the hydrodynamic characteristic time.

Even though the latter assumptions can be commonly found in literature, the reader may find the collisionless assumption in contradiction with the local thermodynamical assumption. As shown in [4], in strongly magnetized plasma, i.e., $\tau_\alpha \Omega_\alpha \gg 1$, the condition for local thermal equilibrium is $\lambda_\alpha / L_\parallel$. Where τ_α is the characteristic collisional time, Ω_α the gyrofrequency, λ_α the mean free path and $L_\parallel$ is the characteristic macroscopic length in the direction of the magnetic field.

However, in the context of multi-fluid modelling, one needs to make the difference between the like particle and different particle collisions. In the current paper, we refer as τ_{ei} to the collisional time between the electrons being scattered by ions. The order of magnitude of the collisional frequencies is:

$$\tau_{ee}^{-1} \sim \tau_{ei}^{-1} \sim \frac{\omega_{pe}}{n\lambda_D^3} \sim \frac{n}{T^{3/2} m_e^{1/2}}, \tag{13}$$

$$\tau_{ii}^{-1} \sim \tau_{ee}^{-1} \sim \frac{\omega_{pi}}{n\lambda_D^3} \sim \left(\frac{m_e}{m_i}\right)^{1/2} \tau_{ee}^{-1} \qquad \text{and} \qquad \tau_{ie}^{-1} \sim \frac{m_e}{m_i}\tau_{ei}^{-1}. \tag{14}$$

With the previous expressions, it can be understood that the energy transferred by an electron to an ion in a collision produces a change in ion's energy that is very small compared to its own energy as the mass ratio is very small. However, the ions may produce a change in the electron's energy that is comparable to the energy transferred in a collision with another electron. Additionally, the effect of the collisions may be negligible in the limit $n\lambda_D^3 \to \infty$, i.e., when the particles in the Debye sphere tend to infinity.

Because of the analysis shown above, we can conclude that the collisionless limit and the local thermal equilibrium assumption seem to be in contradiction. However, in the following we will use the collisionless ideal two-fluid model as an intermediate step towards a more consistent model, since it can be a practical tool to verify the code and retrieve analytical solution.

3 THE IDEAL COLLISIONLESS TWO-FLUID EQUATIONS

3.1 Maxwell equations coupled to multi-fluid equations

In the present section, we give a summary of the equations solved in the results presented herein. In the following, we use the * subindex in order to denote dimensional variables. We present the ideal collisionless multi-fluid equations. Considering N_s, the number of species in plasma, the conservation laws for the species α read:

$$\frac{\partial \rho_\alpha^*}{\partial t^*} + \vec{\nabla}^* \cdot (\rho_\alpha^* \vec{u}_\alpha^*) = 0, \tag{15}$$

$$\frac{\partial \rho_\alpha^* \vec{u}_\alpha^*}{\partial t^*} + \vec{\nabla}^* \cdot (\rho_\alpha^* \vec{u}_\alpha^* \vec{u}_\alpha^* + p_\alpha^* \bar{\bar{I}}) = Q_\alpha^* \vec{E} + \vec{j}_\alpha^* \times \vec{B}^*, \tag{16}$$

$$\frac{\partial \mathcal{E}_\alpha^*}{\partial t} + \vec{\nabla} \cdot (\rho_\alpha^* H_\alpha^* \vec{u}_\alpha^*) = \vec{j}_\alpha^* \cdot \vec{E}^*. \tag{17}$$

As it is shown in the above equations, each species has its own density ρ_α^*, velocity $\vec{u}_\alpha^*$, total energy $\mathcal{E}_\alpha^* = \rho_\alpha^* \frac{{u_\alpha^*}^2}{2} + \mathcal{U}_\alpha^*$ and total enthalpy $H_\alpha^* = \frac{{u_\alpha^*}^2}{2} + h_\alpha^*$ .The charged species have the electric charge Q_α^* and the electric current $\vec{j}_\alpha^* = Q_\alpha^* n_\alpha^* \vec{u}_\alpha^*$.

The previous equations are coupled to Maxwell's equations that describe the spatial and time evolution of the electric field $\vec{E}^*$ and the magnetic induction $\vec{B}^*$. In order to fulfill the two elliptic constraints contained in the Gauss' law and the Gauss' law for magnetism, the divergence cleaning method suggested by Munz et al. [21] is used in the present work. In the mentioned method, two Lagrange multipliers, Ψ and Φ, are introduced to couple the constraints with the evolution equations. The set of equations reads:

$$\frac{\partial \vec{B}^*}{\partial t^*} + \vec{\nabla}^* \times \vec{E}^* + \gamma^2 \vec{\nabla}^* \Psi^* = 0, \tag{18}$$

$$\frac{\partial \vec{E}^*}{\partial t^*} - {c^*}^2 \vec{\nabla}^* \times \vec{B}^* + (\chi c^*)^2 \vec{\nabla} \Phi^* = -\frac{\vec{j}^*}{\epsilon_0^*}, \tag{19}$$

$$\frac{\partial \Psi^*}{\partial t^*} + {c^*}^2 \vec{\nabla}^* \cdot \vec{B}^* = 0, \tag{20}$$

$$\frac{\partial \Phi^*}{\partial t^*} + \vec{\nabla}^* \cdot \vec{E}^* = \frac{\rho_c^*}{\epsilon_0^*}, \tag{21}$$

where $c^* = 299.8 \cdot 10^6$ m/s is the speed of light, $\epsilon_0^* = 8.854 \cdot 10^{-16}$ F/M is the permittivity of free space, and γ and χ are parameters that control the speed of the waves correcting the errors in the divergence constraints, and the total charge density $\rho_c^* = \sum_{\alpha \in N_s} Q_\alpha^* n_\alpha^*$.

3.2 Normalized equations

The previous set of the equations is written in non-dimensional form. We denote normalized variables without the superscript. We can choose three different dimensionally independent variables to normalize the equations. In the following we will consider p_0, ρ_0 and t_0. We define the following non-dimensional parameters, respectively, the normalized gyroradius, Debye length, collisional time and mass ratio:

$$\hat{r}_L = \frac{m_i^* v_0}{B_0 q_0 l_0}, \quad \hat{r}_D^2 = \frac{\epsilon_0 k_B T_0 m_i^*}{\rho_0 q_0^2} \frac{B_0^2 q_0^2}{m_i^2 v_0^2} \quad \text{and} \quad \lambda_m^e = m_i/m_e \tag{22}$$

Note that the non-dimensional Debye length is normalized with the gyroradius.

The rest of reference dimensions are computed as follows:

$$v_0 = \sqrt{p_0/\rho_0} = v_0^{Th}, \quad l_0 = v_0 t_0, \quad T_0 = p_0/(\rho_0 R_i)$$

$$B_0 = \frac{m_i^* v_0}{q_0 l_0 \hat{r}_L}, \quad E_0 = u_0 B_0$$

Using the previous definitions, the normalized set of equations considering electrons and single ionized ions, reads:

$$\frac{\partial \rho_e}{\partial t} + \nabla \cdot (\rho_e \vec{v}_e) = 0 \tag{23}$$

$$\frac{\partial \rho_e \vec{v}_e}{\partial t} + \nabla \cdot (\rho_e \vec{v}_e \vec{v}_e + p_e) = \frac{\lambda_m^e}{\hat{r}_L} \rho_e q_e \left(\vec{E} + \vec{v}_e \times \vec{B} \right) \tag{24}$$

$$\frac{\partial \mathcal{E}_e}{\partial t} + \nabla \cdot (H_e \vec{v}_e) = \frac{\lambda_m^e}{\hat{r}_L} \rho_e q_e \vec{E} \cdot \vec{v}_e \tag{25}$$

$$\frac{\partial \rho_i}{\partial t} + \nabla \cdot (\rho_i \vec{v}_i) = 0 \tag{26}$$

$$\frac{\partial \rho_i \vec{v}_i}{\partial t} + \nabla \cdot (\rho_i \vec{v}_i \vec{v}_i + p_i) = \frac{1}{\hat{r}_L} \rho_i q_i \left(\vec{E} + \vec{v}_i \times \vec{B} \right) \tag{27}$$

$$\frac{\partial \mathcal{E}_i}{\partial t} + \nabla \cdot (H_i \vec{v}_i) = \frac{1}{\hat{r}_L} \rho_i q_i \vec{E} \cdot \vec{v}_i \tag{28}$$

With the non-dimensional ideal gas laws:

$$p_e = \lambda_m^e \rho_e T_e, \quad p_i = \rho_i T_i \tag{29}$$

The set of non-dimensional Maxwell's equations is:

$$\frac{\partial \vec{B}}{\partial t} + \vec{\nabla} \times \vec{E} + \gamma^2 \vec{\nabla} \Psi = 0, \tag{30}$$

$$\frac{\partial \vec{E}}{\partial t} - \left(\frac{c^*}{v_0}\right)^2 \vec{\nabla} \times \vec{B} + \chi^2 \left(\frac{c^*}{v_0}\right)^2 \vec{\nabla} \Phi = -\frac{1}{\hat{r}_D^2 \hat{r}_L} \left(\rho_i q_i \vec{v}_i + \lambda_m^e \rho_e q_e \vec{v}_e\right), \tag{31}$$

$$\frac{\partial \Psi}{\partial t} + \left(\frac{c^*}{v_0}\right)^2 \vec{\nabla} \cdot \vec{B} = 0, \tag{32}$$

$$\frac{\partial \Phi}{\partial t} + \vec{\nabla} \cdot \vec{E} = \frac{1}{\hat{r}_D^2 \hat{r}_L} \left(\rho_i q_i + \lambda_m^e \rho_e q_e\right) \tag{33}$$

4 LINEAR WAVES IN TWO-FLUID PLASMA

In this section, we present the dispersion relation of linear waves traveling in a two-fluid plasma. The present study sumarizes the study presented in [10]. We consider the waves to travel within a homogeneous background at rest: p_{e_0}, p_{i_0}, $\vec{B}_0$, are constant; $n_{e_0} = n_{i_0}$ are constant, therefore, $\vec{E}_0 = 0$; and, $\vec{u}_{e_0} = \vec{u}_{i_0} = 0$, therefore, $\vec{j} = 0$.

We decompose the evolution of the flow variables as $Q(\vec{x}, t) = Q_0 + \tilde{Q} \exp\left[i\left(\vec{k} \cdot \vec{x} - \omega t\right)\right]$ where the perturbations $\tilde{Q}$ are considered to be small. The system of equations (23)-(33) become a system of algebraic equations for the variables $(\tilde{n}_e, \tilde{\vec{u}}_e, \tilde{p}_e, \tilde{n}_i, \tilde{\vec{u}}_i, \tilde{p}_i, \tilde{\vec{E}}, \tilde{\vec{B}})$. Note that the pressure is used as variable instead of the energy, and also, only four electromagnetic variables are independent as a result of the Gauss' laws. Therefore, in total there are 14 independent variables, i.e., so is the number of types of waves we may expect.

First, we change the reference frame where the unit vector $\vec{e}_3$ is on the direction of the propagation of the waves, $\vec{k}$, the vector $\vec{e}_2$ is in the plane defined by $\vec{k}$ and $\vec{B}$, perpedicular to $\vec{e}_3$, as follows:

$$\vec{e}_1 = \vec{e}_2 \times \vec{e}_3, \qquad \vec{e}_2 = \vec{B} \times \vec{k} / |\vec{B} \times \vec{k}|, \qquad \vec{e}_3 = \vec{k} / |\vec{k}| \tag{34}$$

We also define the angle between the propagation direction and the magnetic field, as θ, and the parameters:

$$\lambda = k_\parallel / k = \cos\theta \qquad \text{and} \qquad \tau = k_\perp / k = \sin\theta. \tag{35}$$

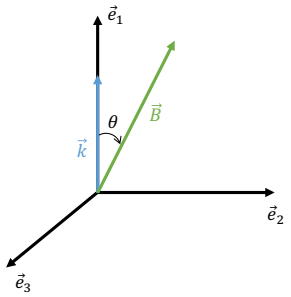

Figure 1: Reference frame used in the study of the wave propagation in two-fluid.

In order to simplify the system of 14 variables, we remove the two marginal waves, i.e., $\omega = 0$. These perturbations, do not move, producing pressure perturbations that compensate the electric field, when $\tilde{n}_e \neq 0$ and $\tilde{n}_i \neq 0$. These pressure perturbations are in counterphase, as follows:

$$\tilde{p}_e = -\tilde{p}_i = i\frac{en_e}{k}\tilde{E}_3 = -\frac{e^2 n_e}{\epsilon_0 k^2}\left(\tilde{n}_e - Z\tilde{n}_i\right) \tag{36}$$

In order to find the resting twelve waves, we define the plasma frequency, gyrofrequency and speed of sound as:

$$\omega_{p_{e,i}} = \sqrt{\frac{e^2 n_{e,i}}{\epsilon_0 m_{e,i}}}, \qquad \Omega_{e,i} = \frac{eB}{m_{e,i}}, \qquad v_{e,i} = \sqrt{\frac{\gamma p_e}{n_{e,i} m_{e,i}}} \tag{37}$$

and the mass ratio as $\mu = m_e/m_i$.

After some transformations, that are omitted in the present paper, the twelve order system reads:

$$\begin{pmatrix} \omega - k^2c^2 & 0 & \omega_{pe}\omega & 0 & -\omega_{pi}\omega & 0 \\ 0 & \frac{\omega^2 - k^2c^2}{-\omega_{pe}^2 - \omega_{pi}^2} & \lambda\omega_{pe}\Omega_e & \tau\omega_{pe}\Omega_e & \lambda\omega_{pi}\Omega_i & \tau\omega_{pi}\Omega_i \\ \omega_{pe}\omega & \lambda\omega_{pe}\Omega_e & \omega^2 - \lambda^2\Omega_e^2 & \lambda\tau\Omega_e^2 & 0 & 0 \\ 0 & \tau\omega_{pe}\Omega_e & -\tau\lambda\Omega_e^2 & \frac{\omega^2 - k^2 v_e^2}{-\omega_{pe}^2 - \tau^2\Omega_e^2} & 0 & \omega_{pe}\omega_{pi} \\ -\omega_{pi}\omega & \lambda\omega_{pi}\Omega_i & 0 & 0 & \omega^2 - \lambda^2\Omega_i^2 & -\lambda\tau\Omega_i^2 \\ 0 & \tau\omega_{pi}\Omega_i & 0 & \omega_{pe}\omega_{pi} & -\lambda\tau\Omega_i^2 & \frac{\omega^2 - k^2 v_i^2}{-\omega_{pi}^2 - \tau^2\Omega_i^2} \end{pmatrix} \cdot \begin{pmatrix} \tilde{E}_1 \\ \tilde{E}_2 \\ \tilde{U}_{e_1} \\ \tilde{U}_{e_3} \\ \tilde{U}_{i_1} \\ \tilde{U}_{i_3} \end{pmatrix} = 0. \tag{38}$$

Taking the determinant of the previous matrix, we retrieve the twelve order polynomial solution for the twelve dispersion relation $\omega = \omega(\vec{k})$. Since the matrix is symmetric, there are six two-fold degerate waves propagating in opposite directions, i.e., $\omega < 0$ and $\omega > 0$.

The polynomial reads, in general form:

$$F(\bar{k}^2, \bar{\omega}^2) = \sum_{m=0}^{6} \sum_{\max(0,3-m)}^{\min(4,6-m)} \alpha_{mn} \bar{k}^{2n} \bar{\omega}^{2m} = 0 \tag{39}$$

where the frequency of the waves and the wave number have been normalized as follows:

$$\bar{\omega} = \omega/\omega_p \quad \text{where} \quad \omega_p = \sqrt{\omega_{pe}^2 + \omega_{pi}^2} \tag{40}$$

$$\bar{k} = \delta k \quad \text{where} \quad \delta = c/\omega_p. \tag{41}$$

The 19 coefficients of the polynomial $\alpha_{mn} = \alpha_{mn}(\lambda^2, \mu, E^2, v^2, w^2)$, depend on the conditions as follows:

$$E = \omega_e/\omega_p, \quad v = v_e/c, \quad \text{and} \quad w = v_i/c. \tag{42}$$

4.1 Waves in the magnetosphere and the solar wind

As we showed in the previous section, the waves in two-fluid plasmas depend strongly on the conditions of the plasma and the direction of propagation. In Table 1, we present the conditions used in this study, corresponding to characteristic conditions in the solar wind and the Earth's magnetosphere.

Table 1: Characteristic conditions in the solar wind and the Earth's magnetosphere.

	Solar wind	Magnetosphere
n	10^7 m^{-3}	10^{10} m^{-3}
B	$6 \cdot 10^{-9}$ T	$3 \cdot 10^{-5}$ T
T	10^5 K	10^4 K
L	$1.5 \cdot 10^6$ m	$6 \cdot 10^3$ m

One of the main interests of studying the wave propagation in two-fluid plasmas is that it contains modes that range from high frequency-short wavelength to slow-long wavelength. As it can be seen in both diagrams of Fig. 2, there are different limits, some of them indicated with dashed lines. The limits are discussed in Table 2.

It can be noted that the dispersion diagrams corresponding to solar wind and magnetosphere conditions are drastically different:

- The upper and lower cutoff limits in the solar wind converge to the plasma frequency, as the ion cyclotron and electron cyclotron frequencies are much smaller than the plasma frequency. However, the upper and lower cutoff is present in the magnetosphere.

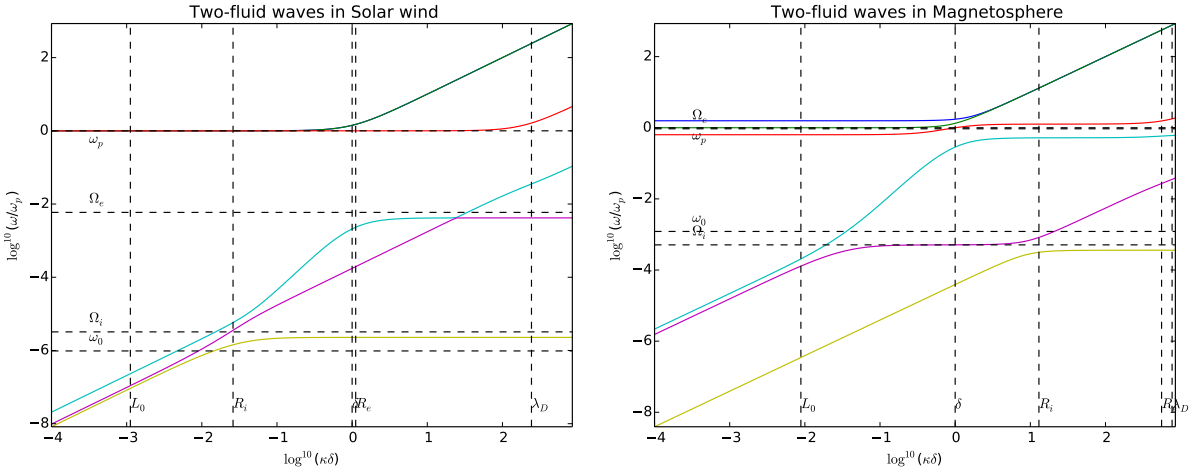

Figure 2: Eigenvalues of the ideal collisionless two-fluid system for oblique propagation at $\theta = 45^o$.

Table 2: Asymptotic limits of the dispersion diagram.

Cutoff $k^2 \to 0$	$\omega^2 = \omega_p^2$ $\omega^2 = \omega_p^2 + \frac{1}{2}(\Omega_e^2 + \Omega_i^2)$ $\pm\lvert\Omega_e - \Omega_i\rvert\sqrt{\omega_p^2 + \frac{1}{4}(\Omega_e + \Omega_i)^2}$	plasma frequency upper and lower cutoff
Resonance $k^2 \to \infty$	$\omega^2 = \lambda\Omega_e^2$ $\omega^2 = \lambda\Omega_i^2$	electron cyclotron ion cyclotron
Local, high frequency $k^2 \to \infty$, $\omega^2 \to \infty$	$\omega^2 = k^2c^2$ $\omega^2 = k^2v_e^2$ $\omega^2 = k^2v_i^2$	EM waves electron sound ion sound
Global, low frequency MHD $k^2 \to 0$, $\omega^2 \to 0$	$\omega^2 = \lambda^2k^2v_A^2$ $\omega^2 = \frac{1}{2}k^2\left[v_A^2 + v_s^2\right.$ $\left.\pm\sqrt{(v_A^2 + v_s^2)^2 - 4\lambda^2v_A^2v_s^2}\right]$	Alfvén slow and fast m.s. wave

- The ion and electron cyclotron limits appear earlier in the solar wind than in the magnetosphere.

- The electromagnetic waves (green line) seem to be closer to the characteristic dimensions (L_0,ω_0) in the magnetosphere than in the solar wind.

- The two-fluid regime seems to be more present in the magnetospheric conditions than in the solar wind, as the solar wind characteristic dimensions are in the MHD

limit, whereas in the magnetosphere comprises higher frequencies.

5 FINITE VOLUME FORMULATION

The presented numerical model is described in [15], studying reactive and collisional multi-fluid cases, while considering the plasma quasi-neutral. We write the system of equations (15)-(21) in conservation form, as follows:

$$\frac{\partial \mathbf{U}(\mathbf{P})}{\partial t} + \vec{\nabla} \cdot \vec{\mathbf{F}}^{(c)} = \vec{\nabla} \cdot \vec{\mathbf{F}}^{(d)} + \mathbf{S}, \tag{43}$$

where $\mathbf{U}$ are the conservative variables and $\mathbf{P}$ are the variables in which we actually store and update the solution. For the Maxwell's system ((18)-(21)), we have:

$$\mathbf{U} = \mathbf{P} = \begin{pmatrix} \vec{B} \\ \vec{E} \\ \hline \Psi \\ \Phi \end{pmatrix}, \ \vec{\mathbf{F}}^{(c)} = \begin{pmatrix} \bar{\bar{I}} \times \vec{E} + \gamma^2 \Psi \bar{\bar{I}} \\ -c^2 \bar{\bar{I}} \times \vec{B} + (\chi c)^2 \Phi \bar{\bar{I}} \\ \hline c^2 \vec{B}^T \\ \vec{E}^T \end{pmatrix} \text{ and } \mathbf{S} = \begin{pmatrix} 0 \\ -\frac{\vec{j}}{\epsilon_0} \\ \hline 0 \\ \frac{\rho_c}{\epsilon_0} \end{pmatrix}. \tag{44}$$

Whereas, for the multi-fluid equations, we consider:

$$\mathbf{U}_s = \begin{pmatrix} \rho_s \\ \rho_s \vec{u}_s \\ \rho_s \mathcal{E}_s \end{pmatrix}, \ \mathbf{P}_s = \begin{pmatrix} \rho_s \\ \vec{u}_s \\ T_s \end{pmatrix}, \ \vec{\mathbf{F}}_s^{(c)} = \begin{pmatrix} \rho_s \vec{u}_s \\ \rho_s \vec{u}_s \vec{u}_s + p_s \bar{\bar{I}} \\ \rho_s H_s \vec{u}_s \end{pmatrix},$$
$$\vec{\mathbf{F}}_s^{(d)} = \begin{pmatrix} 0 \\ \bar{\bar{\pi}}_s \\ \vec{u}_s \cdot \bar{\bar{\pi}}_s - \vec{q}_s \end{pmatrix} \text{ and } \mathbf{S}_s = \begin{pmatrix} \dot{\rho}_s \\ Q_s \vec{E} + \vec{j}_s \times \vec{B} + \sum_{j \neq s}^{j \in N_s} \vec{R}_s^{sj} \\ \vec{j}_s \cdot \vec{E} + \sum_{j \neq s}^{j \in N_s} \dot{Q}_s^{sj} \cdot \vec{u}_s + \sum_{j \neq s}^{j \in N_s} H_s^{sj} + \dot{Q}_s \end{pmatrix}. \tag{45}$$

After writing Eq. (43) in integral form, we can apply the Finite Volume method, as follows:

$$\frac{d\mathbf{U}(\mathbf{P}_i)}{dt} |\Omega_i| + \sum_{j \in \mathscr{D}_i} \mathbf{H}_{ij} |\partial \Omega_{ij}| = \sum_{j \in \mathscr{D}_i} \mathbf{G}_{ij} |\partial \Omega_{ij}| + \mathbf{S}_i |\Omega_i|. \tag{46}$$

The numerical schemes used in the present work, uses modified-CIR for Maxwell's equations, as follows:

$$\mathbf{H}_{ij} = \mathbf{A}_n^+ \mathbf{U}_L + \mathbf{A}_n^- \mathbf{U}_R = \frac{\mathbf{H}(\mathbf{U}_L) + \mathbf{H}(\mathbf{U}_R)}{2} - \frac{1}{2} |\mathbf{A}_n| (\mathbf{U}_R - \mathbf{U}_L), \tag{47}$$

where the numerical diffusivity is scaled in order to balance these terms with the flux terms.

For the multi-fluid equations discretization, a generalization of the AUSM$^+$-up[18] is applied, as follows,

$$\mathbf{H}_s(\mathbf{U}) = \vec{\mathbf{F}}_s^{(c)} \cdot \vec{n} = M_s a_s \begin{pmatrix} \rho_s \\ \rho_s \vec{u}_s \\ \rho_s H_s \end{pmatrix} + p_s \begin{pmatrix} 0 \\ \vec{n} \\ 0 \end{pmatrix}, \tag{48}$$

where the expressions for the upwinded and the pressure fluxes can be found in Liou [18].

Three-point Backward Euler for the second order implicit time discretization, as follows:

$$\mathbf{S}(\tilde{\mathbf{P}}) = \frac{3\mathbf{U}(\tilde{\mathbf{P}}) - 4\mathbf{U}(\mathbf{P}^n) + \mathbf{U}(\mathbf{P}^{n-1})}{2\Delta t} + \mathbf{R}(\tilde{\mathbf{P}}), \tag{49}$$

In order to obtain second-order accuracy in space, we use a weighted linear least square reconstruction [1] with Venkatakrishnan's limiter [25] to obtain second order in space.

6 VALIDATION RESULTS

6.1 Electromagnetic plasma shock

The case studies the evolution of a discontinuity of the plasma density and the magnetic field in one dimension. It is an extension of the Sod tube [23], used to assess the Riemann problem for Euler equations, and especially, the Brio-Wu shocktube [7], used to study the Riemann problem in ideal MHD solvers. The present case, introduced by Shumlak and Loverich [22], studies the same conditions as in the Brio-Wu shocktube, in the multi-fluid limit.

The results presented here are run in a domain extending 50 units with a mesh of 1000 mesh points. The region of interest extends from $x \in [0, 1]$. The domain is chosen to be large enough to avoid having influence of the boundaries, especially when a shock arrives at the boundary. Neumann boundary conditions are chosen for all variables. All the simulations are run until time $t = 0.1$.

The non-dimensional parameters chosen in the results shown herein are : $c^*/v_0 = 100$, $\lambda_m^e = 1836$ and $\hat{r}_D = 0.01$. The normalized gyroradius $\hat{r}_L$ is changed depending on the simulation.

The normalized initial conditions are chosen as follows:

$$\mathbf{P}^{\text{left}}(x<0.5,t=0)=\begin{cases}\vec{B}=(0.75,1,0)\\ \vec{E}=(0,0,0)\\ \Psi=0\\ \Phi=0\\ \rho_e=1/\lambda_m^e\\ \vec{u}_e=(0,0,0)\\ p_e=1/2\\ \rho_i=1\\ \vec{u}_i=(0,0,0)\\ p_i=1/2\end{cases}\qquad \mathbf{P}^{\text{right}}(x>0.5,t=0)=\begin{cases}\vec{B}=(0.75,-1,0)\\ \vec{E}=(0,0,0)\\ \Psi=0\\ \Phi=0\\ \rho_e=0.125/\lambda_m^e\\ \vec{u}_e=(0,0,0)\\ p_e=1/20\\ \rho_i=0.125\\ \vec{u}_i=(0,0,0)\\ p_i=1/20\end{cases} \tag{50}$$

Analogous to the case presented by Shumlak and Loverick [22], we change the value of the normalized gyroradius and we compare to ideal MHD case ($\hat{r}_L \to 0$) and the Euler case ($\hat{r}_L \to \infty$). In Fig. 3, we present the the ion density for the different cases.

The results in Fig. 3 are similar to the ones presented in Shumlak and Loverick [22], although differences are found, maybe due to the different resolution of the mesh or difference in the numerical method. Also, the fact of having a much larger domain is done in order to avoid the reflection of possible waves coming from the boundaries that can play an important role in the solution.

6.2 Flow over a cylinder with complex shock topology

The present case studies the 2-D, field-aligned, low-β and superfast magnetized plasma around a perfectly conducting cylinder. The MHD solution was first calculated in [8]. The main interest of this case is the formation of a shock front with a dimpled shape as it is composed of fast, intermediate and hydrodynamic shock parts. Herein, we reproduce for the first time the previous MHD results with a collisionless ideal two-fluid model.

The results presented here are run in a circular domain of radius 12.5 with a inner circular boundary of radius 0.125. The domain is chosen to be large enough to avoid having influence of the boundaries. Half of the outer boundary is considered as an inlet, whereas the rest is the outlet. At the inlet, the conditions imposed are the ones in Eq. (51), Neumann boundary conditions are chosen for all variables in the outlet, and perfectly conducting walls are chosen for the inner boundary.

The non-dimensional parameters chosen in the results shown herein are as follows: $c^*/v_0 = 100$, $\lambda_m^e = 1836$ and $\hat{r}_D \to 0$. The normalized gyroradius $\hat{r}_L = 0.01$.

The normalized initial and inlet coditions are as follows:

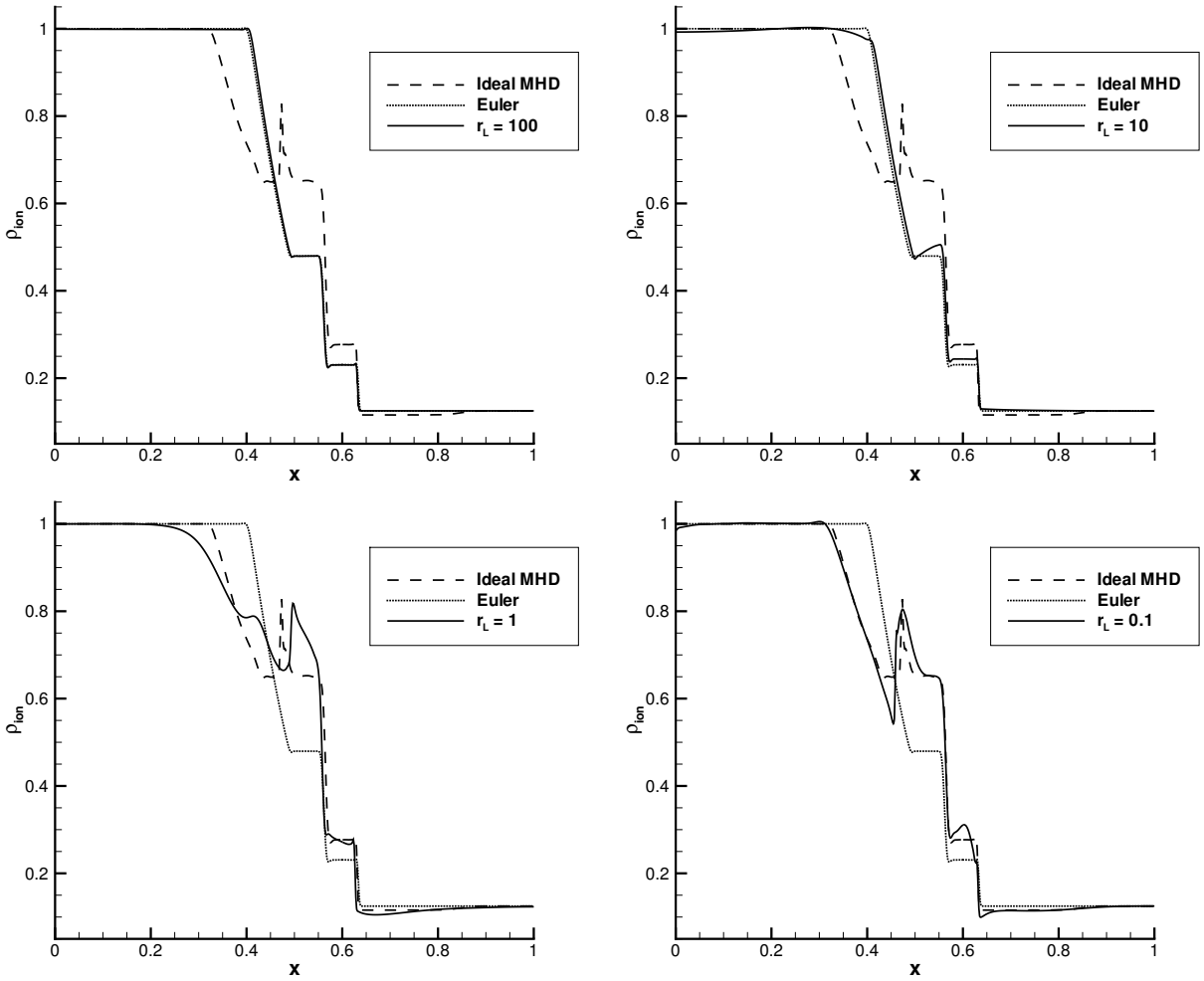

Figure 3: Ion density in the collisionless case for different values of normalized gyroradius.

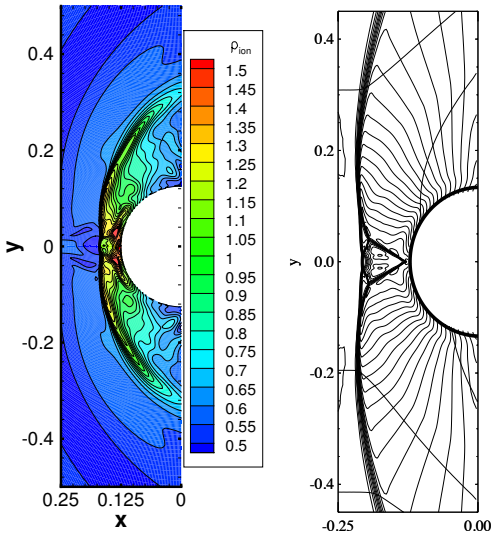

Figure 4: Comparison of the ion density between the two-fluid solution (left) and the MHD solution (right) from [8].

$$\mathbf{P} = \begin{cases} \vec{B} = (1,0,0) \\ \vec{E} = (0,0,0) \\ \Psi = 0 \\ \Phi = 0 \\ \rho_e = 1/\lambda_m^e \\ \vec{u}_e = (1.5,0,0) \\ p_e = 0.1 \\ \rho_i = 1 \\ \vec{u}_i = (1.5,0,0) \\ p_i = 0.1 \end{cases} \tag{51}$$

The two-fluid results compared to the solution of [8] are presented in Fig. 4. Note that in the previous figure, the solution has been rotated in order to be compare so the plasma flows from left to right. Even though, the results of the MHD solution are more evolved, one can note that the characteristic dimple is also present in the collisionless two-fluid solution.

One of the key features of this solution is the use of the real mass ratio. As it can be seen in Eq. (51), the velocity of both species are the same, whereas the mass density of electrons is much smaller since their particle mass is much smaller. Therefore, the speed of sound of electrons is λ_e times higher than the one of the ions. Using the abovementioned initial conditions, the initial Mach number of electrons is subsonic and the one of the ions is supersonic, i.e., $M_e = 0.06$ and $M_i = 2.59$. The Mach of both species are depicted in Fig. 5, showing in both cases the shape of the dimple.

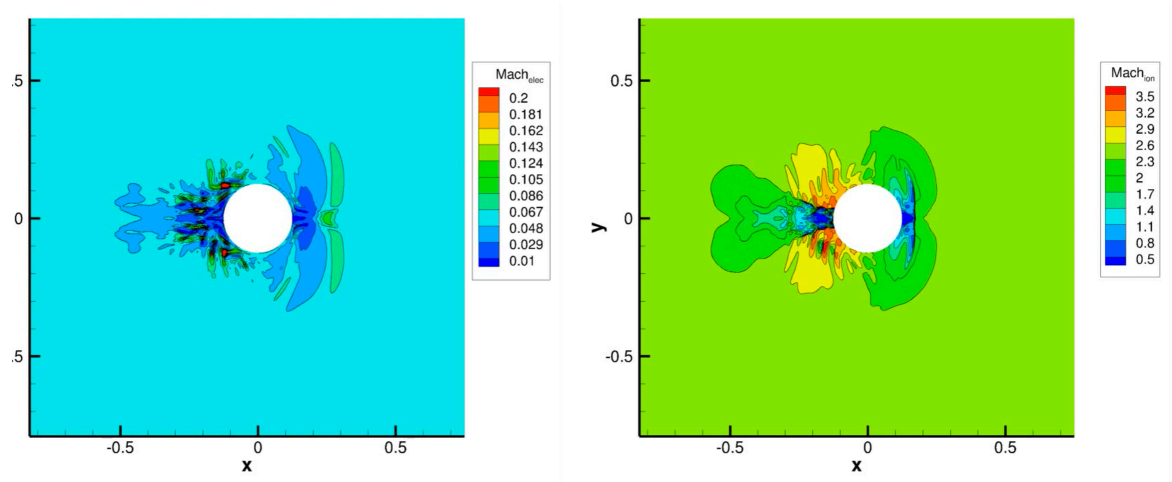

Figure 5: Electron (left) and ion (right) Mach contours. The plasma flows from right to left.

In Fig. 5, one can see the complexity of the wake. In the MHD case, the wake is omitted as only one quarter is simulated. However, in the two-fluid case, the electrons flow subsonically. Therefore, it is not possible to truncate the domain as done in ideal MHD that makes use of supersonic boundary conditions.

6.3 Flow over a sphere with complex shock topology

We extend the results of the previous section in a 3D geometry. In this case, the conditions are the same as in the case of the cylinder, but flowing over a sphere of the same radius. The case is used to verify the 3D implementation of the code.

As in the previous case, we simulate a spherical domain with an inner sphere of radius 0.125. At the inlet, the conditions imposed are the ones in Eq. (51), Neumann boundary conditions are chosen for all variables in the outlet, and perfectly conducting walls are chosen for the inner boundary. The initial field is the one of Eq. (51).

As in the previous case, the non-dimensional parameters chosen in the results shown herein are as follows: $c^*/v_0 = 100$, $\lambda_m^e = 1836$ and $\hat{r}_D \to 0$. The normalized gyroradius $\hat{r}_L = 0.01$.

Preliminary results are presented in Fig. 6. Even though a finer mesh should be tested, the solution shows that also a complex structure forms in the shock front. However, the dimple structure is not as defined as in the 2D case.

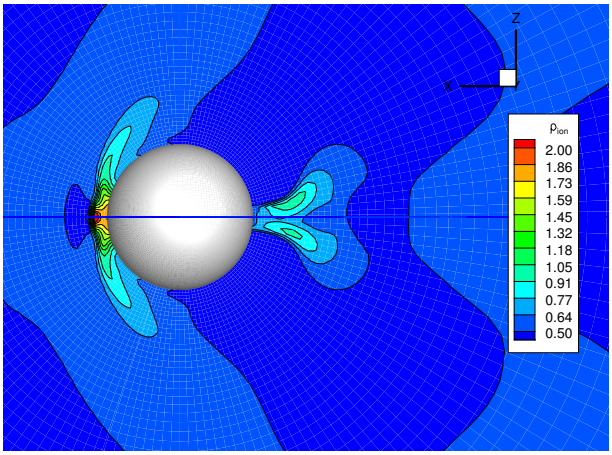

Figure 6: Countour plot of the ion density of the supersonic flow over a sphere. The plasma flows from left to right.

7 MAGNETOSPHERIC RESULTS

7.1 Reconnection in the magnetotail: GEM challenge

Magnetic reconnection plays a fundamental role in the global dynamics of the Earth's magnetosphere. During a geomagnetic substorm, magnetic reconnection takes place in the magnetotail, on the night-side of the magnetosphere, producing heating and acceleration of the particles that travel along the magnetic field lines and can enter the Earth's atmosphere through the polar caps, producing the Northern lights.

Magnetic reconnection in weakly collisional plasmas, as the one in the magnetotail, is a very complex phenomena, where the reconnection can iniciate at scales of the order of the electron's skin depth and that is dominated by the ion's scales. Since reconnection is observed to occur faster than the theoretical models, the simulation community proposed the Geospace Environmental Modeling (GEM) [3] Reconnection Challenge in order to compare the different models representing a collisionless reconnection. Different models, as resistive MHD [3], Hall MHD [19], full-particle and hybrid [30] have been compared in the previous study.

Two-fluid model, as it resolves the electromagnetic and the electron scales, is a good candidate to represent the origins of the reconnection [11]. Magnetic field lines are not frozen in the electron fluid, allowing for reconnection. Therefore, unlike Hall-MHD, two-fluid model does not need an artificial resistivity to initiate reconnection.

The initial conditions consider a Harris current sheet in the z-direction formed by anti-parallel magnetic fields in the x-direction. The magnetic pressure is balanced by the pressure in the plasma pressure (both in electrons and ions, to conserve charge neutrality). The electric current is achieved by an initial diamagnetic velocity in ions and electrons in the z-direction with opposite directions. We also include a small perturbation in the magnetic field, forming two magnetic islands. The initial field reads:

$$\mathbf{P}(\vec{x}, t=0) = \begin{cases} \vec{B} = (B_0 \tanh(y/\lambda) - B_0 \frac{l_0 \pi}{10 L_y} \cos(2x\pi/L_x) \sin(y\pi/L_y), \\ \qquad 2B_0 \frac{l_0 \pi}{10\pi L_x} \sin(2x\pi/L_x) \cos(y\pi/L_y), 0) \\ \vec{E} = (0,0,0) \\ \Psi = 0 \\ \Phi = 0 \\ \rho_e = m_p n_0 \left(1/5 + \operatorname{sech}^2(y/\lambda)\right) \\ \vec{u}_e = (0, 0, \frac{2k_B T_e}{\lambda q B_0} \frac{\operatorname{sech}^2(y/\lambda)}{(1/5 + \operatorname{sech}^2(y/\lambda))}) \\ T_e = \frac{5}{12\mu_0} \frac{B_0^2}{n_0 k_B} \\ \rho_i = m_e n_0 \left(1/5 + \operatorname{sech}^2(y/\lambda)\right) \\ \vec{u}_i = (0, 0, -\frac{2k_B T_i}{\lambda q B_0} \frac{\operatorname{sech}^2(y/\lambda)}{(1/5 + \operatorname{sech}^2(y/\lambda))}) \\ T_i = \frac{1}{12\mu_0} \frac{B_0^2}{n_0 k_B} \end{cases} \tag{52}$$

The non-dimensional parameters chosen in the results shown herein are as follows: $c^*/v_0 = 10$, $\lambda_m^e = 25$ and $\hat{r}_D = 0.0001$. The normalized gyroradius $\hat{r}_L = 1$. In this case, the mass ratio has been chose to this unnatural large value as it was prescribed in the GEM challenge, in order to compare the results with the kinetic simulations.

In Fig. 7, the evolution of the electron and ion momentum is presented. As it can be seen, as the reconnection evolves, the dynamics of electrons and ions decouple from each other. As well, it is worth noting the turbulent structures that appear in the ions flow. These turbulent structures are not seen in any other model, neither in MHD nor in kinetic simulations.

7.2 Preliminary global magnetospheric results

Here we present preliminary results of the first 3D two-fluid magnetospheric result. The computational domain is a sphere of radius 250 with an inner sphere of radius 2.5 centered in the origin. The Geocentric Solar Magnetospheric (GSM) system of coordinates is used for which the x-direction points at the Sun and the dipole is contained in the xz-plane. The outer boundary is divided into two semispheres, one considered as an inlet and the other as the outlet. The inlet imposes the conditions of the solar wind and the outlet applies a Neumann condition. In the inner boundary, the plasma number density is fixed to 56 AMU/cm^3, the temperature is set to 35000 K, and perfectly conducting boundary is applied for the electromagnetic field and mirror for the rest of variables.

As done in [16], the magnetic field is divided into two components: $\vec{B} = \vec{B}_0 + \vec{B}_1$, where $\vec{B}_0$ is a curl-free steady component and $\vec{B}_1$ is the induced component. The curl-free part correspond to the dipole of the Earth, that is set with a tilt angle of 11.94^o.

The initial conditions are taken from measurements of the solar wind performed by the ACE satellite. The initial conditions that coincide with the inlet conditions, read:

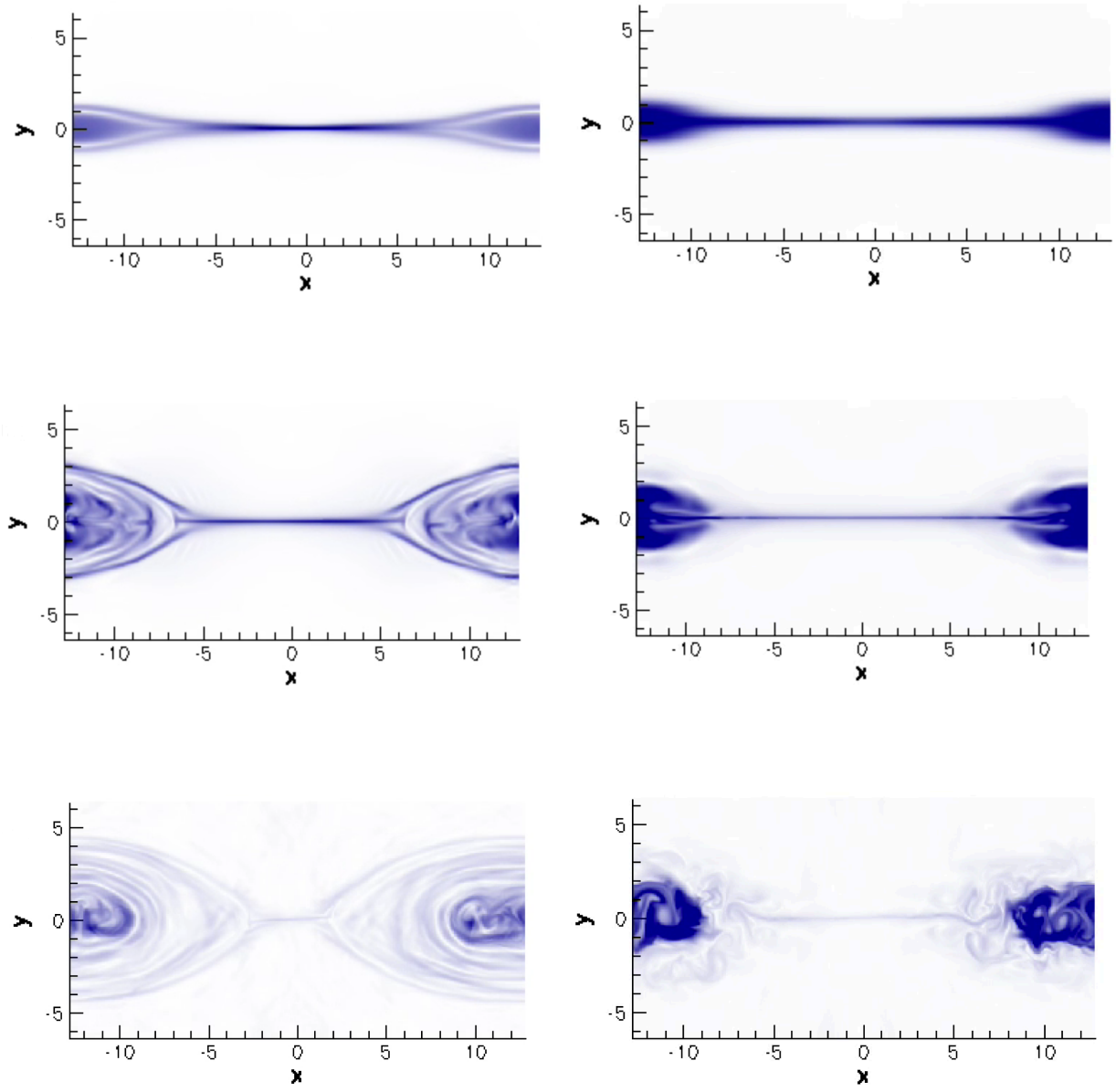

Figure 7: Electron (left) and ion momentum (right) evolution during the magnetic reconnection. Snapshots at $t = 18$ (top), $t = 26$ (middle), $t = 45$ (bottom) panel.

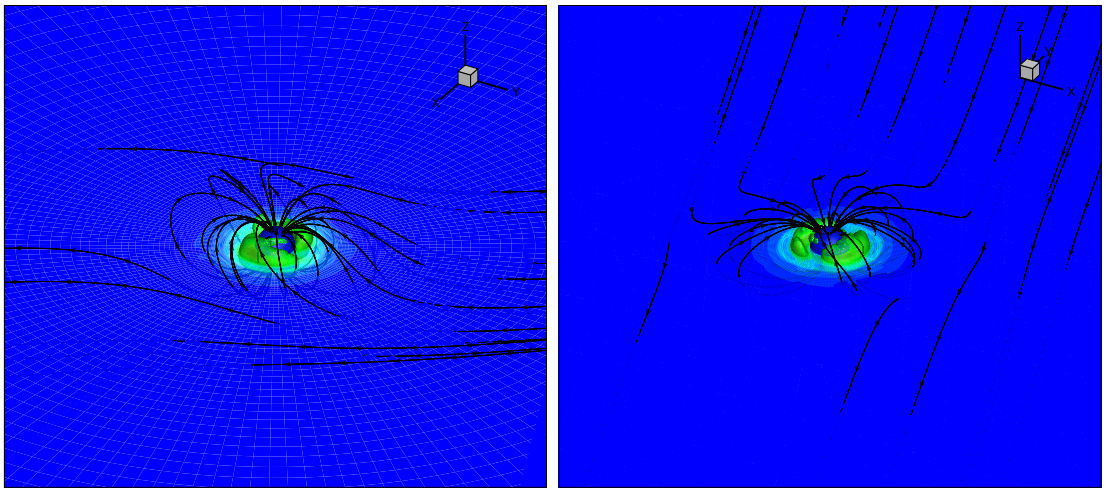

Figure 8: Formation of the ring current in the two-fluid magnetospheric simulation. Contour correspond to the electric current and the lines to the magnetic field.

$$\mathbf{P}(\vec{x}, t=0) = \begin{cases} \vec{B} = (0.591792, -2.13282, -0.602181)\vec{E} = (0,0,0) \\ \Psi = 0 \\ \Phi = 0 \\ \rho_e = 1.26020/\lambda_m^e \\ \vec{u}_e = (-10.8434, -0.859678, 0.0146937) \\ p_e = 0.282599 \\ \rho_i = 1.26020 \\ \vec{u}_i = (-10.8434, -0.859678, 0.0146937) \\ p_i = 0.282599 \end{cases} \tag{53}$$

The non-dimensional parameters chosen in the results shown herein are as follows: $c^*/v_0 = 10$, $\lambda_m^e = 1836$ and $\hat{r}_D = 0.0001$. The normalized gyroradius $\hat{r}_L = 0.1$.

In Fig. 8, the preliminary results of the previous model representing a global magnetosphere are presented. The plots show the magnetic field lines comprising the magnetic dipole of the Earth. Also, the electric current can be seen, forming the so-called ring current around the planet. The results are still at an early stage of the simulation when the bow shock is still not formed.

8 CONCLUSIONS

In the present paper, we present a computational model based on the multi-fluid description oriented to space weather simulations. The ideal collisionless two-fluid plasma model, considering electrons and ions under the effect of electromagnetic fields, has been studied as a first step. The model has been derived from kinetic theory, taking special attention on the assumptions performed at the particle scales in order to retrieve the ideal

collisionless two-fluid model.

The propagation of waves in two-fluid plasmas has been studied. The dispersion diagrams for solar wind and magnetospheric conditions has been presented. Two-fluid plasmas are able to reproduce phenomena ranging from high frequency and small scale dynamics related to the particle dynamics to low frequency and large scale phenomena related to the MHD description. The magnetospheric conditions suggest that the waves present at the relevant scales are in the two-fluid regime rather than in the MHD limit.

The equations have been discretized in a finite volume solver that couples multi-fluid set of equations with Maxwell's equations. The latter is a very stiff system difficult to solve numerically and it solved using a second order implicit time stepping. Second order accuracy in space is obtained by flux reconstruction using flux limiter.

The algorithmic is tested to study the electromagnetic plasma shock problem. Also, the supersonic flow over a cylinder with a complex shock structure is studied. The problem is designed for the first time as two-fluid plasma case. The results show that the dimple in the shock, that was formed in the MHD case is also present in the two-fluid case. The case is extended to 3D showing also a complex shock structure when a sphere is present.

The numerical model is used to study the dynamics of plasmas under magnetospheric conditions. The magnetic reconnection taking place in the magnetotail is studied standalone. The two-fluid description reveals separation of the motion of ions and electrons, as well as turbulent motions that are not present in other descriptions. Preliminary results of a global two-fluid magnetospheric simulation are shown. The two-fluid description is able to represent the ring current in the first stages of the simulation.

AKNOWLEDGEMENTS

The first author would like to thank the teams of UCAR and NASA Ames for the organization of the summer program. The first author's contribution is supported by a Ph. D. grant from the Agency for Innovation by Science and Technology in Flanders (IWT). The third author's contribution was supported by the FWO G.0729.11N grant from the Research Foundation of Flanders. These results were obtained in the framework of the projects GOA/2015-014 (KU Leuven), G.0A23.16N (FWO-Vlaanderen) and C 90347 (ESA Prodex).

REFERENCES

[1] T. Barth. Aspects of unstructured grids and finitevolume solvers for the euler and navier-stokes equations, 1994.

[2] M. S. Benilov. A kinetic derivation of multifluid equations for multispecies nonequilibrium mixtures of reacting gases. *Phys. Plasmas*, 4, 1997.

[3] J. Birn, J. F. Drake, M. A. Shay, B. N. Rogers, R. E. Denton, M. Hesse, M. Kuznetsova, Z. W. Ma, A. Bhattacharjee, A. Otto, and P. L. Pritchett. Geospace

Environmental Modeling (GEM) magnetic reconnection challenge. *Journal of Geophysical Research: Space Physics*, 106:3715–3720, Mar. 2001.

[4] D. Biskamp. *Magnetic Reconnection in Plasmas*. Cambridge Monographs on Plasma Physics. Cambridge University Press, 2000.

[5] G. Borrini, J. T. Gosling, S. J. Bame, and W. C. Feldman. Helium abundance enhancements in the solar wind. *Journal of Geophysical Research: Space Physics*, 87(A9):7370–7378, 1982.

[6] S. I. Braginskii. Transport Processes in a Plasma. *Reviews of Plasma Physics*, 1:205, 1965.

[7] M. Brio and C. C. Wu. An upwind differencing scheme for the equations of ideal magnetohydrodynamics. *Journal of Computational Physics*, 75:400–422, Apr. 1988.

[8] H. de Sterck, B. C. Low, and S. Poedts. Complex magnetohydrodynamic bow shock topology in field-aligned low-β flow around a perfectly conducting cylinder. *Physics of Plasmas*, 5:4015–4027, nov 1998.

[9] A. Glocer. Multifluid block-adaptive-tree solar wind roe-type upwind scheme: Magnetospheric composition and dynamics during geomagnetic storms—initial results. *Journal of Geophysical Research: Space Physics*, 114(A12203):n/a–n/a, 2009.

[10] J. P. H. Goedbloed and S. Poedts. *Principles of Magnetohydrodynamics*. Aug. 2004.

[11] A. Hakim and U. Shumlak. Two-fluid physics and field-reversed configurationsa). *Physics of Plasmas*, 14(5):055911, May 2007.

[12] P. Janhunen, M. Palmroth, T. Laitinen, I. Honkonen, L. Juusola, G. Facskó, and T. I. Pulkkinen. The gumics-4 global mhd magnetosphere-ionosphere coupling simulation. *Journal of Atmospheric and Solar-Terrestrial Physics*, 80:48–59, may 2012.

[13] J. C. Kasper, M. L. Stevens, A. J. Lazarus, J. T. Steinberg, and K. W. Ogilvie. Solar wind helium abundance as a function of speed and heliographic latitude: Variation through a solar cycle. *The Astrophysical Journal*, 660(1):901, 2007.

[14] E. A. Kronberg, M. Ashour-Abdalla, I. Dandouras, D. C. Delcourt, E. E. Grigorenko, L. M. Kistler, I. V. Kuzichev, J. Liao, R. Maggiolo, H. V. Malova, K. G. Orlova, V. Peroomian, D. R. Shklyar, Y. Y. Shprits, D. T. Welling, and L. M. Zelenyi. Circulation of heavy ions and their dynamical effects in the magnetosphere: Recent observations and models. *Space Science Reviews*, 184(1):173–235, 2014.

[15] A. A. Laguna, A. Lani, N. N. Mansour, H. Deconinck, and S. Poedts. A fully-implicit finite-volume method for multi-fluid reactive and collisional magnetized plasmas on unstructured meshes. *Journal of Computational Physics*, doi:10.1016/j.jcp.2016.04.058, 2016.

[16] A. Lani, M. S. Yalim, and S. Poedts. A gpu-enabled finite volume solver for global magnetospheric simulations on unstructured grids. *Computer Physics Communications*, 185(10):2538–2557, 2014.

[17] W. Lennartsson, R. D. Sharp, E. G. Shelley, R. G. Johnson, and H. Balsiger. Ion composition and energy distribution during 10 magnetic storms. *Journal of Geophysical Research: Space Physics*, 86(A6):4628–4638, 1981.

[18] M.-S. Liou. A sequel to AUSM, Part II: AUSM$^+$-up for all speeds. *Journal of Computational Physics*, 214:137–170, May 2006.

[19] Z. W. Ma and A. Bhattacharjee. Hall magnetohydrodynamic reconnection: The Geospace Environment Modeling challenge. *Journal of Geophysical Research: Space Physics*, 106:3773–3782, Mar. 2001.

[20] E. T. Meier and U. Shumlak. A general nonlinear fluid model for reacting plasma-neutral mixtures. *Physics of Plasmas*, 19(7):072508, July 2012.

[21] C.-D. Munz, P. Ommes, and R. Schneider. A three-dimensional finite-volume solver for the Maxwell equations with divergence cleaning on unstructured meshes. *Computer Physics Communications*, 130:83–117, July 2000.

[22] U. Shumlak and J. Loverich. Approximate riemann solver for the two-fluid plasma model. *J. Comput. Phys.*, 187(2):620–638, May 2003.

[23] G. A. Sod. A survey of several finite difference methods for systems of nonlinear hyperbolic conservation laws. *Journal of Computational Physics*, 27:1–31, Apr. 1978.

[24] G. Tóth, I. V. Sokolov, T. I. Gombosi, D. R. Chesney, C. R. Clauer, D. L. De Zeeuw, K. C. Hansen, K. J. Kane, W. B. Manchester, R. C. Oehmke, K. G. Powell, A. J. Ridley, I. I. Roussev, Q. F. Stout, O. Volberg, R. A. Wolf, S. Sazykin, A. Chan, B. Yu, and J. Kóta. Space weather modeling framework: A new tool for the space science community. *Journal of Geophysical Research: Space Physics*, 110(A12):n/a–n/a, 2005.

[25] V. Venkatakrishnan. On the accuracy of limiters and convergence to steady state solutions, 1993.

[26] S. von Alfthana et al. Vlasiator: First global hybrid-vlasov simulations of earth's foreshock and magnetosheath. *Journal of Atmospheric and Solar-Terrestrial Physics*, 120:24–35, december 2014.

[27] G. S. Voronov. Kinetic theory of plasmas: Translational energy. *Mathematical Models and Methods in Applied Sciencess*, 19:527–599, 2009.

[28] R. M. Winglee, W. K. Peterson, A. W. Yau, E. Harnett, and A. Stickle. Model/data comparisons of ionospheric outflow as a function of invariant latitude and magnetic local time. *Journal of Geophysical Research: Space Physics*, 113(A6):n/a–n/a, 2008. A06220.

[29] M. S. Yalim, D. vanden Abeele, A. Lani, T. Quintino, and H. Deconinck. A finite volume implicit time integration method for solving the equations of ideal magneto-hydrodynamics for the hyperbolic divergence cleaning approach. *Journal of Computational Physics*, 230:6136–6154, July 2011.

[30] L. Yin, D. Winske, S. P. Gary, and J. Birn. Hybrid and Hall-MHD simulations of collisionless reconnection: Dynamics of the electron pressure tensor. *Journal of Geophysical Research: Space Physics*, 106:10761–10776, June 2001.

[31] V. M. Zhdanov. Transport Processes in Multicomponent Plasma. *Plasma Physics and Controlled Fusion*, 44:2283, Oct. 2002.